# Half-metallicity and magnetism in the $Co_2MnAl/CoMnVAl$ heterostructure

Igor Di Marco,[1] Andreas Held,[2] Samara Keshavarz,[1] Yaroslav O. Kvashnin,[1] and Liviu Chioncel[2,3]
[1]*Department of Physics and Astronomy, Uppsala University, Box 516, SE-75120 Uppsala, Sweden*
[2]*Theoretical Physics III, Center for Electronic Correlations and Magnetism, Institute of Physics, University of Augsburg, D-86135 Augsburg, Germany*
[3]*Augsburg Center for Innovative Technologies, University of Augsburg, D-86135 Augsburg, Germany*

(Received 29 September 2017; published 4 January 2018)

We present a study of the electronic structure and magnetism of $Co_2MnAl$, CoMnVAl, and their heterostructure. We employ a combination of density-functional theory and dynamical mean-field theory (DFT+DMFT). We find that $Co_2MnAl$ is a half-metallic ferromagnet, whose electronic and magnetic properties are not drastically changed by strong electronic correlations, static or dynamic. Nonquasiparticle states are shown to appear in the minority spin gap without affecting the spin polarization at the Fermi level predicted by standard DFT. We find that CoMnVAl is a semiconductor or a semimetal, depending on the employed computational approach. We then focus on the electronic and magnetic properties of the $Co_2MnAl/CoMnVAl$ heterostructure, predicted by previous first-principle calculations as a possible candidate for spin-injecting devices. We find that two interfaces, Co-Co/V-Al and Co-Mn/Mn-Al, preserve the half-metallic character, with and without including electronic correlations. We also analyze the magnetic exchange interactions in the bulk and at the interfaces. At the Co-Mn/Mn-Al interface, competing magnetic interactions are likely to favor the formation of a noncollinear magnetic order, which is detrimental for the spin polarization.

DOI: 10.1103/PhysRevB.97.035105

## I. INTRODUCTION

In the last decade spintronics has emerged as an important field of research at the intersection between electronics and magnetism [1]. The basic concept in spintronics is that information is transmitted by manipulating not only charge but also spin currents. Applications include various devices, as, e.g., the magnetoresistive random access memory, based on the giant magnetoresistance (GMR) and tunneling magnetoresistance (TMR) phenomena [2,3]. Practical realizations of these effects consist of multilayered systems whose basic components are half-metallic ferromagnets (HMFs) [4–7] sandwiching a nonmagnetic layer (either semiconducting or metallic). In order to realize an efficient spin injection, the HMFs have to be chosen with a high spin polarization, possibly holding over a wide range of temperatures.

Searching for materials with the right properties for spintronics is not a simple task. While experimental studies involve a substantial amount of resources, theoretical investigations suffer from oversimplified modeling, neglecting important factors such as the nonstochiometry of the samples or the presence of defects [8]. Additionally, theoretical studies are often based on density-functional theory (DFT), which treats electronic correlations only approximately in local or semilocal functionals [9–11].

HMFs possess 3*d* electrons that are partially localized and are therefore expected to exhibit significant correlation effects [12]. In fact they are characterized by an essential feature due to many-body effects, i.e., the existence of nonquasiparticle (NQP) states [13–15]. NQP states influence the value and temperature dependence of the spin polarization in HMFs [12,15,16] and are therefore of primary interest for potential applications. NQP states have been shown to contribute significantly to the tunneling transport in heterostructures containing HMFs [17–21], even in the presence of arbitrary disorder. The origin of NQP states is connected with "spin-polaron" processes; in half-metals where the gap appears in the minority spin channel (minority spin gap half-metals) no low-energy electron excitations are possible in the minority spin channel within the single-particle picture. However, low-energy electron excitations can still be constructed as superpositions of spin-up electron excitations and virtual magnons [12–15].

Including NQP states in the electronic structure requires methods beyond standard DFT. The dynamical mean-field theory (DMFT) [22–24] describes the local correlation effects exactly and is therefore suitable to capture the essential physics of the HMFs [12]. To retain the predictive character of *ab initio* calculations one often employs a combination of DFT in the local spin-density approximation (LSDA) and DMFT, which we address here with the acronym LSDA+DMFT (for a review of this approach, see Ref. [25]). The LSDA+DMFT scheme has been successfully applied to describe the physical properties of a variety of HMFs, including systems of both minority spin gap [4,26–30] and majority spin gap [28,31]. The general feature reported in these studies is that NQP states leave their signature on the excitation spectra as small resonances just above (below) the Fermi level when the gap lies in the minority (majority) spin channel. Nonlocal correlations have also been investigated, by means of theories beyond DMFT, as, e.g., the variational cluster approach [32–35]. These calculations not only confirm the main findings obtained with DMFT, but they even assign a larger weight to the NQP states around the Fermi level [29,36,37].

While the depolarizing mechanism associated with NQP states has been widely studied in bulk HMFs, a few studies

 ©2018 American Physical Society

analyzed this phenomenon in multilayered heterostructures which are the components of the GMR/TMR setup. The magnetic tunnel junction $Co_2MnSi/AlO_2/Co_2MnSi$ was investigated by means of tunneling spectroscopy measurements, showing evidence of NQP states above the Fermi level [16]. More recently, the magnetic tunnel junction $Co_2MnSi/MgO$ was analyzed through extremely low energy photoemission spectroscopy [38]. Although these results can be interpreted in terms of NQP states, the authors suggested that they can also be a signature of a noncollinear arrangement of spins at the interface. These experimental findings and the lack of material-specific studies of interfaces based on advanced many-body theories are the motivations behind the present work. To analyze the role of NQP states and the tendency to noncollinear magnetism, we focus on bulk $Co_2MnAl$ and CoMnVAl, as well as their heterostructure. The relevance of these systems lays in the fact that they were previously predicted [39] to form two interfaces preserving the half-metallic character of the parent material $Co_2MnAl$, namely Co-Co/V-Al and Co-Mn/Mn-Al. In the present work we show that this important conclusion is not changed by the inclusion of strong correlation effects. We also show that the Co-Mn/Mn-Al interface is characterized by competing exchange interactions that may potentially lead to a noncollinear arrangement of spins. Our results suggest that the present heterostructure is a good candidate for the experimental realization of a highly spin-polarized interface, in particular if focusing on Co-Co/V-Al.

The paper is organized as follows. Section II illustrates the computational details used for our calculations. Sections III A and III B are dedicated to bulk $Co_2MnAl$ and bulk CoMnVAl, respectively. The magnetic and spectral properties of the heterostructure composed by $Co_2MnAl$ and CoMnVAl are presented in Sec. IV. The conclusions of our work are drawn in Sec. V.

## II. COMPUTATIONAL DETAILS

Scalar relativistic electronic structure calculations were performed by means of the full-potential linearized muffin-tin orbitals (FP-LMTO) code RSPt [40,41]. The exchange-correlation potential was treated in the LSDA and in the generalized gradient approximation (GGA), using respectively the parametrizations by Perdew and Wang [42] and by Perdew, Burke, and Enzerhof [43]. The muffin-tin spheres, which in a full-potential code are still used to divide the physical space in the unit cell, were carefully optimized to offer a good description of the electron density in both bulk and heterostructure. This procedure lead to muffin-tin radii of 2.20, 2.10, 1.8, and 2.34 a.u. for, respectively, Mn, Co, Al, and V. The valence electrons were described with $4s$, $4p$, and $3d$ states for the transition metals and $3s$, $3p$, and $3d$ states for Al. Selected calculations were also performed with an extended set of valence electrons, including semicore states. Considering these additional states resulted into a variation of the equilibrium lattice constants of less than 0.1% and was therefore deemed not necessary for the purposes of this study.

In RSPt one can address the effects of strong Coulomb interaction for localized electrons at the level of LSDA+$U$ [44] and LSDA+DMFT [25]. Both approaches start from a correction to the Kohn-Sham Hamiltonian in the form of an explicit intra-atomic Hubbard repulsion for the $3d$ states of the transition metal elements. This term can then be treated self-consistently in a mean-field (Hartree-Fock) approach, as in LSDA+$U$ [44], or by more sophisticated many-body theories, as in LSDA+DMFT [25]. We here consider the most general form of LSDA+$U$ and LSDA+DMFT, where the interaction vertex is taken as a full spin and orbital rotationally invariant 4-index $U$ matrix [44,45]. This matrix is parametrized in terms of Slater parameters, which are $F^0$, $F^2$, and $F^4$ for $3d$ states. These parameters can in turn be obtained from the average screened Coulomb interaction $U$ and corresponding Hund exchange $J$ [25,46]. Calculated Coulomb interaction parameters were recently reported for $Co_2MnAl$ [47], based on the constrained random-phase approximation (cRPA). The authors reported a partially (fully) screened value of $U$ of 3.40 (0.81) eV for Co and of 3.23 (0.83) eV for Mn. As far as we know, there are no calculations available for CoMnVAl. Therefore, for simplicity and for facilitating a meaningful comparison between bulk and heterostructures, we here adopted a uniform value of $U = 2.0$ eV for the $3d$ states of all transition metals (Mn, Co, and V). This value is included in the range defined by the partially screened value and the fully screened value reported above, and is also in line with the values calculated for the corresponding elemental solids [48,49]. The Hund's exchange $J$ is not affected much by screening and was here set to a value of 0.9 eV. For completeness, we also performed an additional set of calculations by using the partially screened values mentioned above. Those results are summarized in Appendix A.

The addition of a Hubbard $U$ interaction term in the total energy functional, also introduces the need for a "double-counting" correction. The latter accounts for the fact that the contribution to the total energy due to the Hubbard term is already included (although not correctly) in the exchange correlation functional. The double-counting scheme is unfortunately not uniquely defined, and usually creates some ambiguity [50,51]. Here we consider the double counting in the so-called fully localized limit (FLL) [44,50,52] in LSDA+$U$. For LSDA+DMFT we instead remove the orbital average of the static part of the self-energy [46,53,54]. The effective impurity model arising in LSDA+DMFT is solved by means of the relativistic version of the spin-polarized T-matrix fluctuation exchange (SPTF) approximation [53,55]. The applicability of SPTF to HMFs and Heusler compounds has already been demonstrated in a number of studies, as discussed in a recent review [12].

The LSDA+DMFT calculations were performed using finite temperature Green's functions at $T = 160$ K. A total of 2048 Matsubara frequencies were considered. Spectral functions for all methods were calculated at real energies displaced at a distance $\delta = 2$ mRy from the real axis. In case of LSDA+DMFT the analytical continuation of the self-energy was required to obtain the spectral function. To this aim we used the least-square average Padé approximant method [56], whose initial steps are based on Beach's formulation [57]. In the following, for an easier comparison with electronic structure literature, we will drop the term spectral function in favor of density of states (DOS) and projected density of states (PDOS). The local orbitals used to describe the $3d$ states in LSDA+$U$ and LSDA+DMFT were constructed from the

so-called muffin-tin (MT) heads and are therefore atomiclike. A more comprehensive discussion on this and other technical details can be found in Refs. [46,54,58].

We have also calculated the exchange parameters between the magnetic atoms in the bulk and at the interface of the two compounds. Using the converged electronic density obtained in the previous step, the interatomic exchange parameters were obtained by mapping the magnetic excitations onto the Heisenberg Hamiltonian:

$$\hat{H} = -\sum_{i \neq j} J_{ij} \vec{e}_i \vec{e}_j, \tag{1}$$

where $J_{ij}$ is an exchange interaction between the spins at sites $i$ and $j$, and $\vec{e}_i$ is a unit vector along the magnetization direction at the corresponding site. We extracted the $J_{ij}$'s by employing the method of infinitesimal rotations of the spins in the framework of the magnetic force theorem [59,60]. More technical details about the evaluation of the exchange interactions in RSPt can be found in Ref. [61]. The local orbitals used to calculate the $J_{ij}$'s were again chosen as MT heads.

While we used RSPt for all data presented in this article, the geometry optimization of the heterostructure was too heavy to be performed in an all-electron method. Therefore, to this aim, we employed the projector augmented wave method [62], as implemented in the VASP code [63]. The plane-wave energy cutoff was set to 550 eV to ensure the completeness of the basis set. The positions of the ions as well as the volume were relaxed so that the residual forces between the ions became less that 0.01 eV/Å. Meanwhile, the lattice constant in the $xy$ plane as well as in the $z$ direction have been varied separately around the averaged of the optimized bulk values for $Co_2MnAl$ and CoMnVAl, until the change in the total energy was found converged up to 0.001 eV.

## III. BULK

### A. The half-metallic $Co_2MnAl$

$Co_2MnAl$ [64] is a type of Heusler compound which crystallizes in the cubic $L2_1$ structure (space group $Fm\bar{3}m$). The Co atoms are placed on Wyckoff position $8c/(1/4,1/4,1/4)$, while Mn and Al atoms are situated in the position $4a(0,0,0)$ and $4b(1/2,1/2,1/2)$, respectively. We performed relaxation of the lattice constant in GGA, which usually leads to a good description of the chemical bonding in transition metals compounds. The Brillouin zone (BZ) was sampled with a dense Monkhorst-Pack grid of $16 \times 16 \times 16$ **k** points. We obtained an equilibrium lattice constant of 5.69 Å, which coincides with the value reported in a recent study based on a pseudopotential plane-wave code [65]. This value is in reasonable agreement with the experimental value of 5.75 Å [64], which confirms that our approach can describe the structural properties well.

We then performed an analysis of magnetic and spectral properties at the equilibrium volume in LSDA, LSDA+$U$, and LSDA+DMFT. The spin-resolved DOS and PDOS for the $3d$ states of Mn and Co in the three methods are reported in Fig. 1. In plain LSDA $Co_2MnAl$ is a half-metal with a gap in the minority spin channel of about 0.6 eV, consistent with previous literature [66,67]. The region of low-energy excitations, around the Fermi level, is dominated by the $3d$ states of the transition

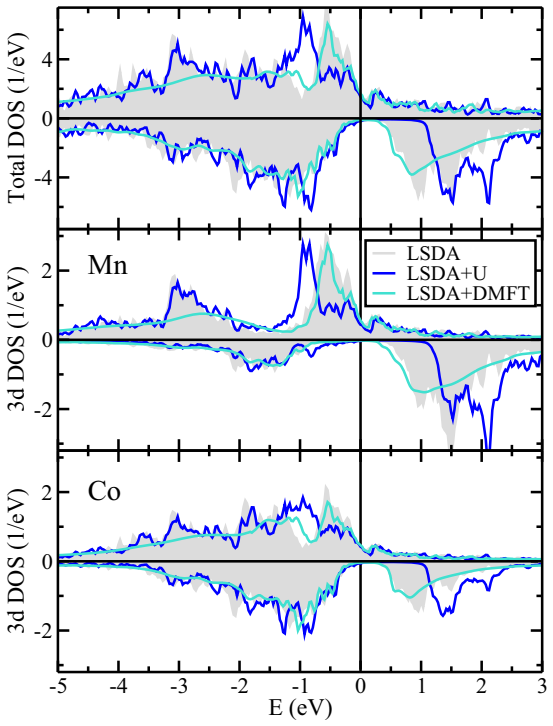


FIG. 1. Total DOS of $Co_2MnAl$, as well as PDOS for the $3d$ states of Mn and Co, as obtained in LSDA (gray shade), LSDA+$U$ (blue), and LSDA+DMFT (turquoise). Positive and negative values correspond to majority and minority spin channels, respectively. The Fermi level is at zero energy and emphasized with a vertical line.

metals. The $3d$ states of two Co sublattices couple and form bonding hybrids, which also hybridize with the manifold of $3d$ states of Mn, for both $e_g$ and $t_{2g}$ symmetries [12]. This coupling also results in Co-Co antibonding hybrids, which remain uncoupled, owing to their symmetry. Therefore the gap is defined by the triply degenerate Co-Co antibonding hybrids of $t_{2g}$ character and the doubly degenerate Co-Co antibonding hybrids of $e_g$ character. Figure 1 illustrates how the energy gap in the minority spin channel is defined by Co states, while Mn-derived states are characterized by a larger gap of about 1.5 eV.

When adding exchange and correlation effects at the LSDA+$U$ level, one observes an increase of the gap. In the majority spin channel one observes that the large peak of $t_{2g}$ character moves from $-0.5$ eV in LSDA to $-0.9$ eV in LSDA+$U$, while the smaller peaks of $e_g$ character remain pinned at the Fermi level and at around $-3$ eV. In the minority spin channel, instead, both symmetries are affected and the spectrum is almost uniformly shifted upwards of 0.5 eV.

In LSDA+DMFT one obtains a physical picture closer to the one given by standard LSDA than to the one given by LSDA+$U$. With respect to LSDA, two interesting effects are visible. At high energies the spectrum is smeared and shrinked towards the Fermi level, in analogy to what happens in the itinerant ferromagnets Fe, Co, and Ni [46]. Second, at low energies, NQP states appear in the minority spin channel, just above the Fermi energy. These states lead to a smaller gap but do not destroy the half-metallic character. An interesting feature, which is just visible in Fig. 1, is that NQP states affect

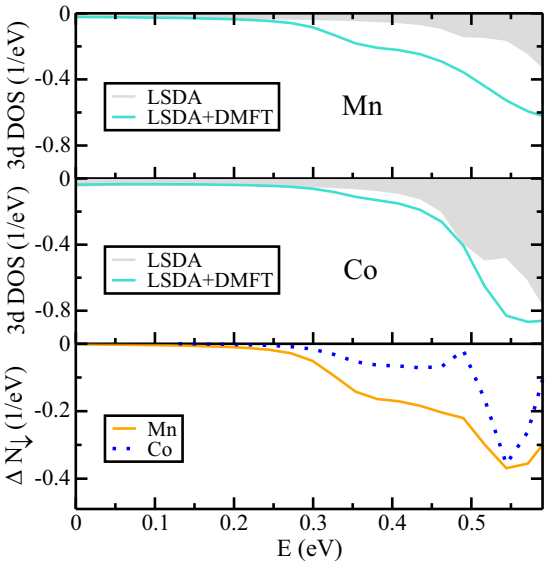


FIG. 2. Minority spin PDOS for the Mn-3$d$ states and for the Co-3$d$ states in $Co_2MnAl$, as obtained in LSDA (gray shade) and LSDA+DMFT (turquoise). Negative values are used to have the same convention as in Fig. 1. The difference $\Delta N_{\downarrow}(E)$ between the PDOS obtained in LSDA and LSDA+DMFT for each set of states is also shown, in the bottom panel. The Fermi level is at zero energy.

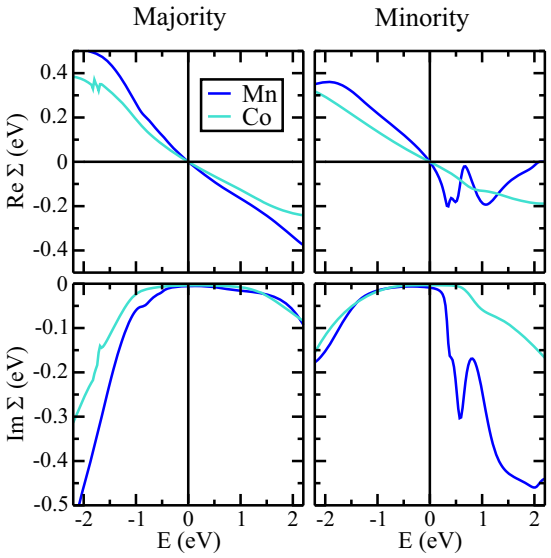


FIG. 3. Average self-energy per orbital of the Mn-3$d$ states and Co-3$d$ states in $Co_2MnAl$, separately for majority (left panels) and minority (right panels) spin channels. Both real and imaginary parts are reported, respectively, in the top and bottom panels. The Fermi level is at zero energy and emphasized with a vertical line.

mainly Mn-3$d$ states, while the effects at the Co sites is much reduced. This can be seen better in Fig. 2, where the minority spin PDOS curves shown in Fig. 1 are enlarged in the closest region above the Fermi energy. A more quantitative measure of this asymmetry between Mn and Co can be seen in the bottom panel of Fig. 2, where the difference $\Delta N_{\downarrow}(E)$ between the minority spin PDOS obtained in LSDA+DMFT and the one obtained in LSDA is reported. The large negative peak at about 0.5 eV is due to the shift of the band edge, but the shoulder at 0.3–0.4 eV can be ascribed to NQP states. The effects on NQP states on the spectrum at the Mn site are about 5 times larger than those on the spectrum at the Co sites. The signature of NQP states is particularly evident in the orbitally averaged self-energy function, which is reported in Fig. 3. In the minority spin channel, the imaginary part of the Mn self-energy is characterized by a large peak appearing at 0.4 eV above the Fermi level, while only a small shoulder is visible for Co. This is in sharp contrast with the majority spin channel, where curves have similar shapes. One can also notice that the magnitude of the corrections induced by the self-energy for Mn is much bigger than for Co. This is in agreement with studies on the transition metal elements, where correlation effects were shown to be the larger, the closer the 3$d$ shell is to half-filling, i.e., the larger the magnetic moment [54]

Magnetic properties can be analyzed through the total and site-projected magnetic moments, which are reported in Table I, for LSDA, LSDA+$U$, and LSDA+DMFT. While LSDA and LSDA+DMFT lead to similar values, in LSDA+U one can see that the moment at the Mn site is increased, which is compensated by an increase of the antiparallel moment in the interstitial region (in between the muffin-tin spheres). This change is not determined by the redistribution of the total charge in between the two regions but by a genuine increase of the exchange splitting. This remodulation is also accompanied by a smaller change of magnetic moment at the Co sites.

Using the electronic structure obtained in LSDA, LSDA+$U$, and LSDA+DMFT, we calculated interatomic exchange parameters $J_{ij}$'s. Results are shown in Fig. 4. In bulk $Co_2MnAl$, the $J_{ij}$'s decay quite fast with the interatomic distance and therefore the dominant coupling is the nearest-neighbor ferromagnetic interaction between Co and Mn atoms. The present feature is in good agreement with prior DFT studies [68] and is independent of the method used for treating correlation effects. Consistently with the PDOS (Fig. 1), the $J_{ij}$'s obtained from LSDA and LSDA+DMFT are quite similar to each other, whereas LSDA+$U$ results show larger differences. The dominant Co-Mn coupling is enhanced in LSDA+$U$, which reflects the increase of the magnetic moment reported in Table I.

### B. The semiconducting CoMnVAl

CoMnVAl crystallizes in the $Y$ structure (LiMgPdSn type, $F\bar{4}3m$ symmetry; see, e.g., Ref. [69]), where the Wyckoff positions 4$a$(0,0,0), 4$b$(1/2,1/2,1/2), 4$c$(1/4,1/4,1/4), and 4$d$(3/4,3/4,3/4) are respectively occupied by Mn, Co, Al, and V. It can be synthesised as a solid solution by mixing $Mn_2VAl$

TABLE I. Site-projected and total magnetic moments for bulk $Co_2MnAl$, as computed in LSDA, LSDA+$U$, and LSDA+DMFT. The values are given in $\mu_B$.

| | $\mu_{Mn}$ | $\mu_{Co}$ | $\mu_{Al}$ | $\mu_{int}$ | $\mu_{cell}$ |
|---|---|---|---|---|---|
| LSDA | 2.48 | 0.81 | −0.03 | −0.07 | 4.00 |
| LSDA+$U$ | 2.63 | 0.79 | −0.04 | −0.17 | 4.01 |
| LSDA+DMFT | 2.46 | 0.82 | −0.03 | −0.08 | 4.00 |

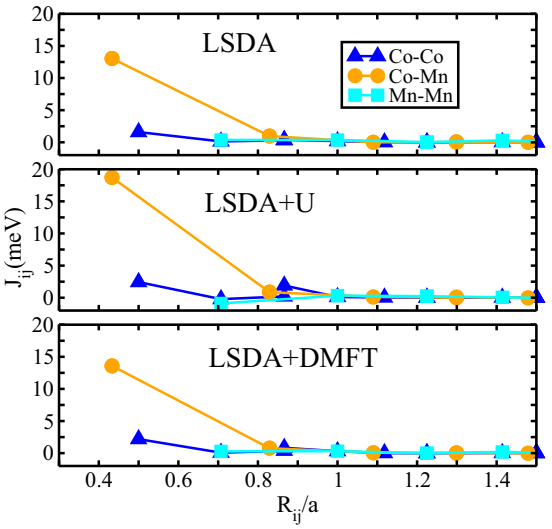


FIG. 4. Interatomic exchange parameters $J_{ij}$ between all magnetic atoms in bulk $Co_2MnAl$ as given by LSDA, LSDA+$U$, and LSDA+DMFT. Interatomic distances are expressed in units of the equilibrium lattice constant.

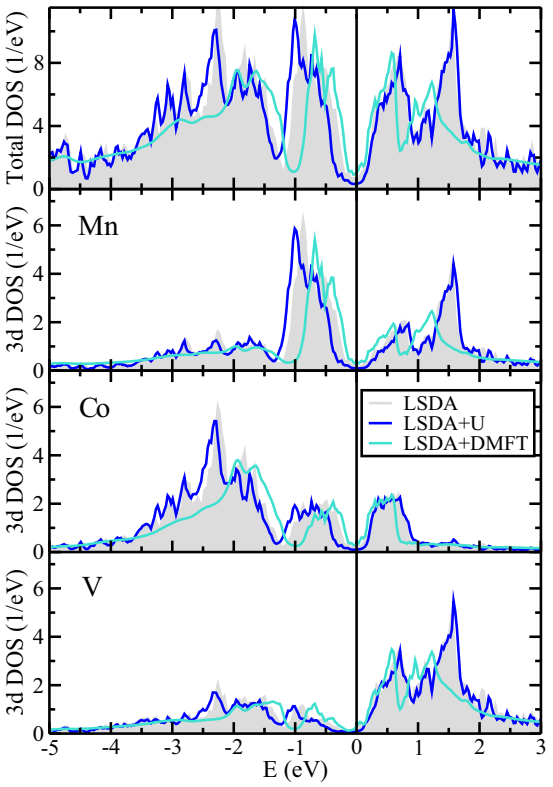


FIG. 5. Total DOS of CoMnVAl, as well as PDOS for the 3$d$ states of Mn, Co, and V, as obtained in LSDA (gray shade), LSDA+$U$ (blue), and LSDA+DMFT (turquoise). Only the total trace is shown, since the system is nonmagnetic. The Fermi level is at zero energy and emphasized with a vertical line.

and $Co_2VAl$ in equal amount [70]. The primitive cell contains 24 valence electrons and, according to the Slater-Pauling rule [71,72], should be expected to be a semiconductor (SC), either magnetic or nonmagnetic [73]. Among the quaternary Heusler compounds, one is more likely to find small-gap SCs, since the unit cell contains three different transition metals [74]. CoMnVAl was in fact predicted to be a nonmagnetic SC through first-principles calculations [39,74], although the presence of an indirect negative gap formally makes it a semimetal [39,73]. The lattice constant measured in experiments amounts to 5.80 Å [70], which is rather close to that of $Co_2MnAl$. These characteristics make CoMnVAl and $Co_2MnAl$ suitable to be grown in heterostructures useful for spintronics [39].

As for $Co_2MnAl$, we performed relaxation of the lattice constant in GGA. The BZ was again sampled with a dense Monkhorst-Pack grid of $16 \times 16 \times 16\,\mathbf{k}$ points. We obtained an equilibrium lattice constant of 5.74 Å, which is in line with the values obtained with a pseudopotential plane-wave method [75] and with a full-potential linearized augmented plane-wave (FP-LAPW) method [73], respectively, 5.76 and 5.74 Å. The calculated lattice constant is in reasonable agreement with the experimental value reported above, leading to an error of about 1%.

In the ground state there are no finite magnetic moments, consistently with previous literature. The spin-integrated DOS and PDOS of CoMnVAl are reported in Fig. 5, for LSDA, LSDA+$U$, and LSDA+DMFT. The data obtained in LSDA show a small amount of states at the Fermi energy. The origin of these states is clarified by inspecting the LSDA band structure, reported in the top panel of Fig. 6. The valence band crosses the Fermi level at the Γ point, while the conduction band goes below it at the $X$ point. These semimetallic features have been reported in prior works [39,73]. Further insight into the band structure can be obtained by analyzing projections over real spherical (cubic) harmonics (data not shown). One can identify that the contribution at the Γ point arises from Mn and Co $t_{2g}$ states, while at the $X$ point there are mainly V-$e_g$ states. The latter hybridize with Mn and Co $e_g$ orbitals to form the conduction band extending from $X$ to Γ.

In LSDA+$U$ CoMnVAl turns into a proper SC. This is not fully visible in Fig. 5, due to the smearing used for printing DOS and PDOS (see Sec. II). Nevertheless, the band structure reported in the middle panel of Fig. 6 shows this feature unambiguously. The formation of an indirect band gap along the Γ-$X$ direction is due to the fact that the V-$e_g$ states (together with the corresponding hybridizing states of Co and Mn) are pushed upwards by the Hubbard $U$ correction and become completely unoccupied.

The physical picture emerging from LSDA+DMFT calculations is more complex. The mechanism which leads to the opening of a band gap in LSDA+$U$ is in fact counteracted by the fact that the occupied 3$d$ states are pushed upwards. This is clear in both Fig. 5 and in the bottom panel of Fig. 6, especially around the Γ point. As a consequence, the top of the valence band, corresponding to Mn and Co $t_{2g}$ states, almost touches the conduction band, corresponding to Mn and Co $e_g$ states. In the bottom panel of Fig. 6 one can also observe that at high excitation energies the band structure is no longer well defined, due to shorter quasiparticle lifetimes arising from electron-electron interaction.

A more quantitative analysis of the changes induced by the three computational methods can be made by extracting the $\Gamma \rightarrow X$ band gap from Fig. 6. In LSDA we obtain a value

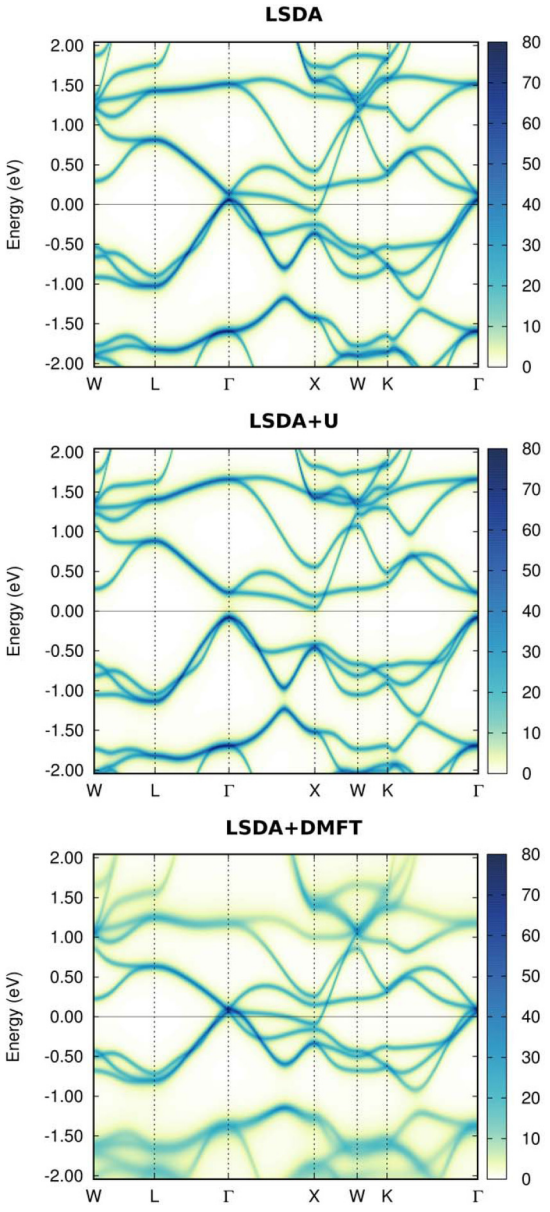


FIG. 6. Total spectral densities of CoMnVAl along high-symmetry directions in the Brillouin zone, as obtained in LSDA, LSDA+$U$, and LSDA+DMFT. The Fermi level is at zero energy.

of −0.14 eV, which is in fair agreement with the value of −0.07 eV obtained in GGA with a FP-LAPW code [73]. In LSDA+DMFT, instead, we obtain a value of −0.21 eV, which corresponds to a variation of around 0.07 eV with respect to the LSDA value. This change is identical to the one obtained in $GW$ with respect to standard GGA, as presented in Ref. [73]. $GW$ data are also similar to our LSDA+DMFT results in the reduction of the direct band gap at $X$ point, with respect to standard DFT. Conversely the direct band gap at the Γ point is increased in $GW$, while almost vanishes in our LSDA+DMFT simulations. Since the impurity solver used here (SPTF) contains diagrammatic contributions that are similar to those included in $GW$, we can attribute the observed discrepancies to the fact that DMFT neglects nonlocal fluctuations, while they are included in $GW$. Overall, however, our data agrees well with previous literature.

In the following, for simplicity, we will refer to CoMnVAl as a SC, although it is such only in LSDA+$U$.

## IV. HALF-METALLIC INTERFACE

As discussed in the Introduction, HMFs are usually incorporated in spintronic devices in the form of films or multilayers and therefore it is important to address the properties of these systems. De Wijs and de Groot [76] were the first authors to investigate surfaces and interfaces of HMFs in search for good candidates for spin injection. Although they found out that surfaces and interfaces of HMFs are by construction prone to a loss of spin polarization, they also identified NiMnSb/CdS (111) as a system preserving the half-metallicity of its parent material. Later, various studies addressed the problem of interfacing HMFs with different types of SCs in the search of good heterostructures for spintronics [77–82]. The presence of interface states reducing (or even inverting) the spin polarization has been explained as due to the lack of the $d$-$d$ hybridization at the interface, which leaves $d$-like dangling bond states inside the gap [83]. To solve this problem, Chadov *et al.* [39] suggested that Heusler alloys have such a rich variety of physical properties that one may attempt to construct interfaces where both the HMF and the SC are Heusler alloys. This would make it possible to preserve the nature of the bonding through the interface, which may potentially preserve the complete spin polarization. $Co_2MnAl$ and CoMnVAl were chosen as the two fundamental components for the interface. Among all possible stackings, Co-Co/V-Al and Co-Mn/Mn-Al were identified as energetically favorable interfaces which preserve the half-metallic character, and therefore suitable for experimental realization [39].

In this section we aim to explain under what conditions the coherence of the bonding through the interface remains persistent against the effects of electron correlations. We performed electronic structure calculations of the heterostructure composed by $Co_2MnAl$ and CoMnVAl. We considered a supercell of 64 atoms (32 atoms for each component) aligned along the (001) direction, as illustrated in Fig. 7. The structure was first fully relaxed in GGA by means of the VASP code, as described above. The BZ was sampled with a dense Monkhorst-Pack grid of $8 \times 8 \times 2$ **k** points, which lead to total energies converged up to 0.1 meV. The equilibrium lattice constant of the heterostructure is of about 5.718 Å, which is roughly the average of the optimized bulk values reported above, and is in good agreement with the results by Chadov *et al.* [39]. The relaxed structure was used as an input for electronic structure calculations with RSPt. For those, the BZ was sampled with a dense Monkhorst-Pack grid of $8 \times 8 \times 1$ **k** points.

### A. Magnetic properties

First, we focus on the magnetic moments per atomic site in LSDA, which are reported in Fig. 8. For convenience, also the magnetic moments per layer are shown (thick black line). At the Co-Co/V-Al interface, the symmetry of the Co sites is broken as they acquire two different magnetic moments. These moments are slightly smaller than those at the Co sites

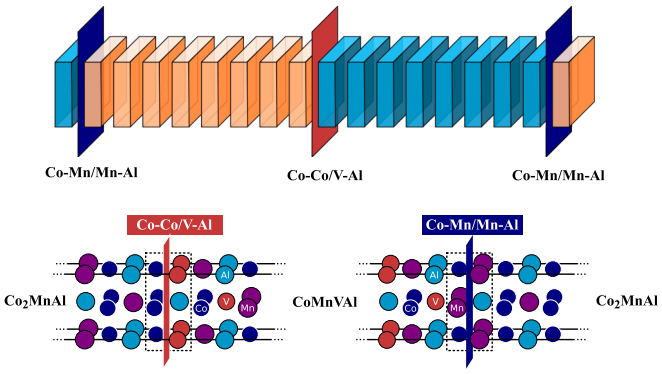


FIG. 7. Supercell composed by eight unit cells of the HMF $Co_2MnAl$ (orange blocks) and by eight unit cells of the SC CoMnVAl (turquoise blocks). The supercell contains two distinct interfaces, namely Co-Co/V-Al (red plane) and Co-Mn/Mn-Al (blue plane), whose composition is shown in the lower panels. The atoms of Mn, Co, Al, and V are, respectively, represented by violet, blue, turquoise, and red spheres.

in the innermost layer, which in turn reproduces the bulk properties quite well (see Appendix B). On the SC side of the interface, the exchange coupling with the Co-3*d* states induces a small moment at the V site. In the next layer, the moments on Co and Mn align antiparallel to each other, leading to a small total moment. The nonmagnetic character of the bulk is practically recovered from the fourth layer and beyond. For the Co-Mn/Mn-Al interface, on the HMF side, one observes a 10% decrease of the moment at the Mn site with respect to its bulk value. In the second layer, instead, the moments at the Co sites are slightly larger than in the bulk. As in the Co-Co/V-Al interface, they also exhibit a symmetry breaking, although not so evident. On the SC side, at the interface, one observes the formation of an induced moment at the Co site. The presence of a large antiparallel moment at the Mn site results in a total moment per layer which is antiparallel to the total magnetization. The moments per layer on the SC side of the interface are ordered antiferromagnetically along the (001) direction. This is slightly different than what happens at the Co-Co/V-Al interface, where interfacial effects cause the first layer (V-Al) and the second layer (Co-Mn) to have parallel moments orientation.

The LSDA results reported in Fig. 8 are similar to the ones obtained by Chadov *et al.* [39]. As a general tendency, the moments at the transition metals sites seem to be slightly larger in our study than in theirs. This is partly due to intrinsic reasons, i.e., the existence of discrepancies between the electron densities calculated in a full-potential (FP) scheme versus the atomic-sphere approximation (ASA), used respectively in this work and in Ref. [39]. The usage a FP scheme is expected to be important especially for the layers at the interface. However, we expect that another reason why we report larger moments with respect to Ref. [39] is the fact that we use slightly smaller muffin-tin spheres to obtain locally projected quantities. In fact, in ASA one is required to use overlapping spheres to cover the full physical space, including the interstitial regions between different atoms, while in a FP scheme the interstitial region is treated separately.

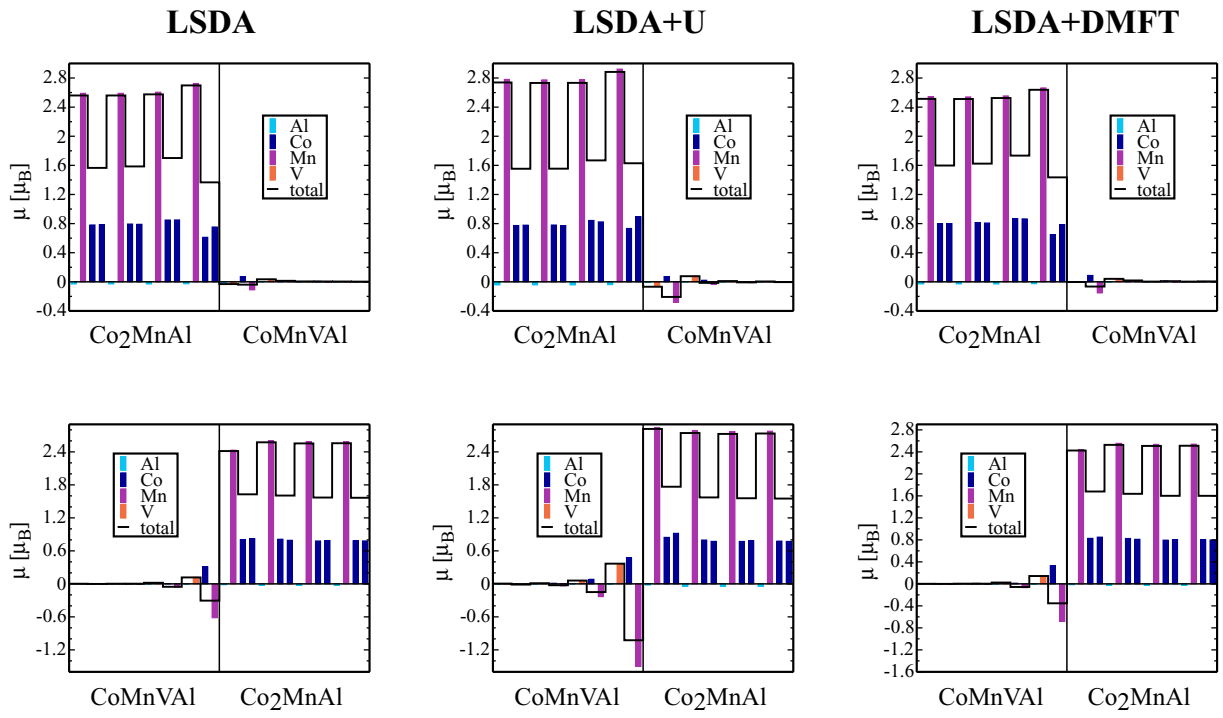


FIG. 8. Trends of the magnetic moments across the interface in LSDA, LSDA+$U$, and LSDA+DMFT. The top panels refer to the Co-Co/V-Al interface, while the bottom panels refer to the Co-Mn/Mn-Al interface. The $x$ axis indicates the different layers along the (001) direction. The moment per layer is given by the thick black line, while the colored bars indicate the moment at each atomic site within a layer. The colors are set using the same convention of the atomic spheres of Fig. 7.

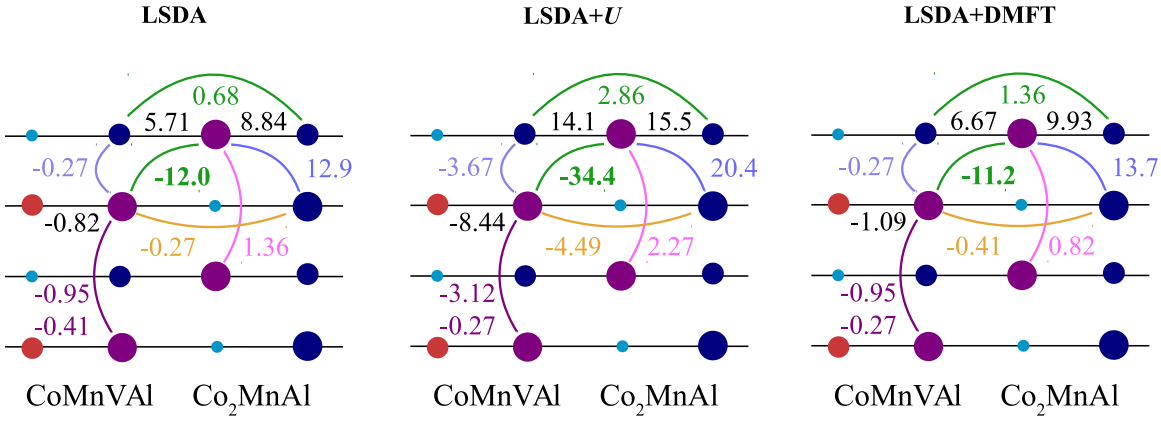


FIG. 9. Interatomic exchange parameters $J_{ij}$ in meV for the most relevant atomic pairs at the interface Co-Mn/Mn-Al. Mn, Co, V, and Al atoms are, respectively, represented as violet, blue, red, and turquoise spheres. Different exchange parameters are reported with respect to their interatomic bonds (in the same colors). Bigger circles represent atoms belonging to $xz$ plane with $x = 0.0$, while small circles represent atoms belonging to the plane with $x = 0.5$. The $z$ axis is perpendicular to the interface plane as in other plots. Notice that two different numbers are reported for the Mn-Mn bond on the side of interface containing CoMnVAl. These numbers refer to two different directions which are indistinguishable in a two-dimensional plane. The upper and lower numbers correspond to bonds along the [100] and [010] directions, respectively.

In Fig. 8 one can also observe the magnetic moments obtained in LSDA+$U$ and LSDA+DMFT. The physical picture obtained in these two approaches is rather similar to the one obtained in plain LSDA. Including correlation effects leads to an increase of the magnetic moments at the transition metal atoms. The increase is more marked in LSDA+$U$ than in LSDA+DMFT and is particularly evident for the Mn and V sites on the SC side of both interfaces. For example the moment at the Mn (V) site in LSDA+$U$ is about 2.5 (3.2) times larger than in LSDA. In fact, in LSDA+$U$, the magnitude of the V moment in the second layer of the Co-Mn/Mn-Al interface is comparable to that of the Co moment in the first layer. Another interesting observation is that in LSDA+$U$ the moments of the Co sites close to the interface become larger than those in the bulk, while in LSDA and LSDA+DMFT the situation is reversed.

Finally, we have calculated the exchange parameters for the heterostructure. We did not consider the Co-Co/V-Al interface because of the negligible magnetic moments at the SC side. The dominant $J_{ij}$'s at the Co-Mn/Mn-Al interface are instead reported in Fig. 9. The most interesting magnetic interactions are the ones across the interface. In particular, the largest coupling happens between two Mn atoms at the opposite sides of the interface and is antiferromagnetic (green bold number), which is also reflected by the antiparallel moment observed in Fig. 8. We stress that this strong antiferromagnetic coupling emerges only at the interface, since in the bulk of $Co_2MnAl$, Mn ions are only second nearest neighbors of each other (see Fig. 4). This interaction is also particularly affected by the inclusion of strong correlation effects and in LSDA+$U$ becomes even larger than the Co-Mn nearest-neighbor coupling that drives the ferromagnetic order of the bulk HMF. The Co-Mn interaction across the interface (black line in Fig. 8) is ferromagnetic, but weaker than the aforementioned Mn-Mn coupling. Furthermore, the $J_{ij}$ between Co and Mn on the CoMnVAl side of the interface (purple line) is antiferromagnetic, but relatively small, even in LSDA+$U$. Again on the CoMnVAl side of the interface, one can see the presence of a small antiferromagnetic coupling between Mn and V (black lines). This coupling increases of an order of magnitude in LSDA+$U$, reaching a strength comparable with the other magnetic interactions. As discussed for the magnetic moments, LSDA+DMFT results in magnetic couplings that are very similar to those obtained in standard LSDA.

Within the current magnetic configuration all the magnetic interactions seem satisfied, suggesting that the chosen magnetic order is locally stable. However, the $J_{ij}$'s extracted by the magnetic force theorem are known to depend on the reference state. Thus, we believe that there are two indications that the current magnetic order might not be the ground state. First, the Co and Mn moments on the CoMnVAl side are quite small in magnitude; second, the $J_{ij}$ between them is surprisingly small. Our interpretation is that this coupling (indicated by a purple line in Fig. 9) might actually be ferromagnetic. However, since it is in competition with a strong antiferromagnetic Mn-Mn coupling and a strong ferromagnetic Co-Mn coupling across the interface, the system finds it energetically favorable to suppress these magnetic moments. To verify this hypothesis we performed additional calculations by removing the HMF from the supercell. As a matter of fact, we obtain (data not shown) that the corresponding magnetic moments are ferromagnetically coupled and become strongly enhanced. This situation may potentially lead to a noncollinear spin order, which has already been suggested for interfaces involving Heuslers alloys [38]. A more quantitative analysis of such ordering could be done by performing simulations based on atomistic spin dynamics [84,85], but this task is beyond the scope of the present study.

### B. Spectral properties

We now focus on the half-metallic character (or lacking of) at the interfaces. In Fig. 10 the PDOS for the 3$d$ states of the transition metals at the Co-Co/V-Al interface are reported.

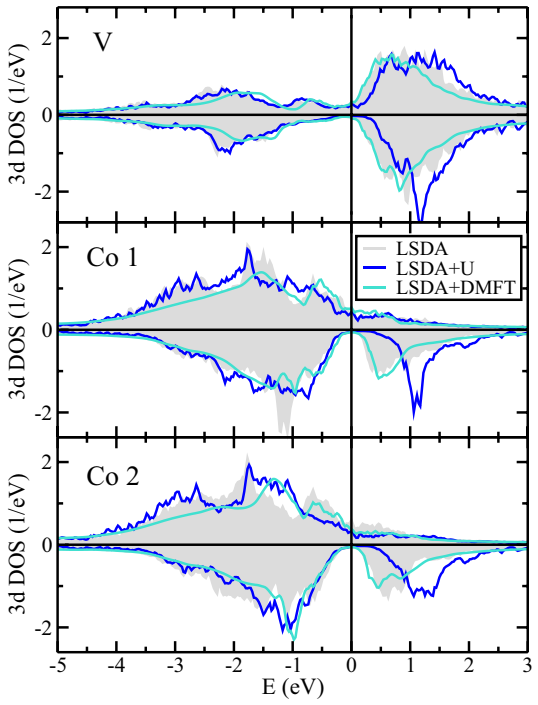


FIG. 10. PDOS for the 3*d* states of V and Co (both types) at the interface Co-Co/V-Al, as obtained in LSDA (gray shade), LSDA+$U$ (blue), and LSDA+DMFT (turquoise). V belongs to the SC side of the interface, while Co1 and Co2 are located in the HMF side. Positive and negative values correspond to majority and minority spin channels, respectively. The Fermi level is at zero energy and emphasized with a vertical line.

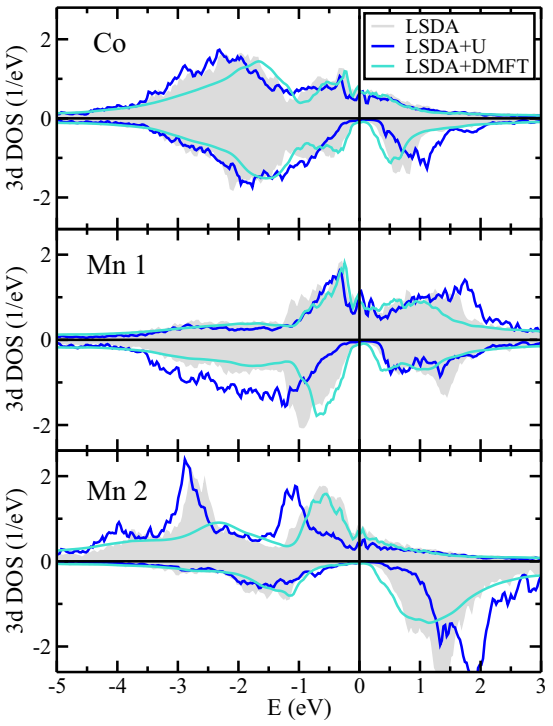


FIG. 11. PDOS for the 3*d* states of Co and Mn (both types) at the interface Co-Mn/Mn-Al, as obtained in LSDA (gray shade), LSDA+$U$ (blue), and LSDA+DMFT (turquoise). Co and Mn1 belong to the SC side of the interface, while Mn2 is located in the HMF side. Positive and negative values correspond to majority and minority spin channels, respectively. Notice that the magnetic moment at the Mn 1 site is antiparallel to the global magnetization, therefore there are more electrons with minority spin character than majority spin character. The Fermi level is at zero energy and emphasized with a vertical line.

The minority-spin band gap is preserved in all computational approaches, but becomes particularly large in LSDA+$U$. It is interesting to see that the corrections induced by the Hubbard terms are much larger at the Co site with the largest moment (bottom panel of Fig. 10) than at the Co site with the smallest moment (middle panel of Fig. 10). The corresponding self-energies of the Co-3*d* states (data not shown) are very similar to the bulk values of $Co_2MnAl$, with no evident signature of NQP states. We can then move to the Co-Mn/Mn-Al interface, whose PDOS for all relevant states are reported in Fig. 11. Also in this case all approaches preserve the half-metallic character. In LSDA+$U$ one observes an increase of the band gap as well as of the exchange splitting. In LSDA+DMFT, one observes similar features as in the bulk $Co_2MnAl$, even for the Mn site at the SC side of the interface ("Mn 1" in Fig. 11). Notice that the local magnetization axis at this site is different than the global magnetization axis, because of the negative magnetic moment (see Fig. 8). For both Mn types at the interface the tail due to the NQP states extends closer to the Fermi level than in the bulk HMF, resulting in a 35% reduction of the band gap with respect to its LDA value.

The inspection of the self-energy, reported in Fig. 12, reveals that the NQP state appears only at the Mn site belonging to the HMF side of the interface. With respect to the bulk $Co_2MnAl$, the NQP state is shifted closer to the Fermi level, which reflects a stronger reduction of the band gap, mentioned above. Conversely the self-energy at the Mn site on the SC side of the interface does not show such a feature and its overall similar to the one for the bulk CoMnVAl (data not shown). The only difference concerns the absolute intensity, which for the majority (minority) spin channel is smaller (bigger) than in the bulk. Notice that we again refer to the global magnetization axis.

## V. CONCLUSIONS

In this work we investigate the correlated band structure and magnetism of the $Co_2MnAl$/CoMnVAl heterostructure, as well as its bulk constituents. Bulk $Co_2MnAl$ is shown to be a HMF, whose magnetic moments and exchange couplings depend only mildly on the inclusion of strong electronic correlations (both static and dynamic). In LSDA+$U$, where the largest corrections are observed, the magnetic moments are increased of about 10% with respect to their values in LSDA, while the increase of the nearest neighbor exchange coupling is at most of 40%. No qualitative changes, as, e.g., in the sign of the magnetic moments or the interatomic exchange parameters, are observed. LSDA+DMFT simulations clearly show the appearance of NQP states within the minority-spin gap in the band structure. These states are identified to originate mainly from Mn-3*d* states and are located several hundreds meV above the Fermi level. Therefore, they do not seem to affect

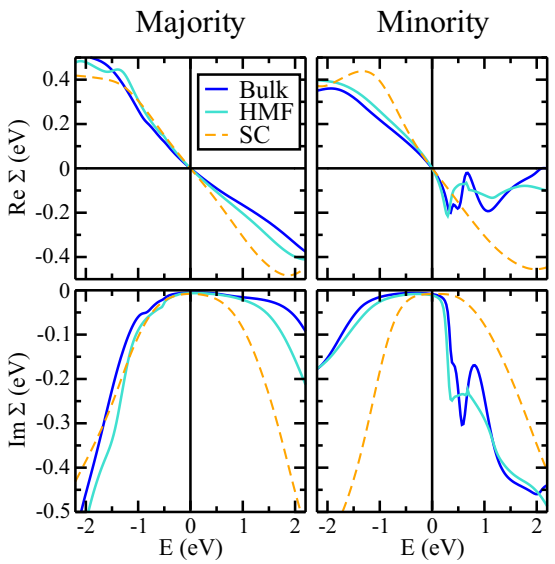


FIG. 12. Average self-energy per orbital of the Mn-3*d* states in $Co_2MnAl$ and at the HMF side of the Co-Mn/Mn-Al interface, separately for majority (left panels) and minority (right panels) spin channels. Both real and imaginary parts are reported, respectively, in the top and bottom panels. The Fermi level is at zero energy and emphasized with a vertical line.

the predicted spin polarization very much. Bulk CoMnVAl is shown to be a semimetal in both LSDA and LSDA+DMFT, while it turns into a proper SC in LSDA+$U$. The scenarios predicted by these three methods are all compatible with experimental observations and previous literature, pointing to a very limited conductivity.

The $Co_2MnAl$/CoMnVAl heterostructure is the most interesting system addressed in this work. In LSDA, two distinct interfaces are predicted to have a half-metallic character, namely Co-Co/V-Al and Co-Mn/Mn-Al. This prediction is not changed by including strong correlation effects, both through LSDA+$U$ or LSDA+DMFT. Our LSDA+DMFT calculations predict the appearance of NQP states at the Co-Mn/Mn-Al interface, but this does not affect the spin polarization at the Fermi energy, similarly to bulk $Co_2MnAl$. The Co-Mn/Mn-Al interface is also interesting for its magnetism. The presence of two Mn atoms which are relatively close to each other leads to a strong antiferromagnetic coupling, which is stabilized by reducing the size of neighboring moments. Although the exchange interactions suggest that the calculated collinear magnetic structure is locally stable, the suppression of some magnetic moments indicates the presence of competing magnetic interactions, which are likely to induce noncollinearity of spins at the interface. The interatomic exchange parameters reported in this work can in principle be used to perform finite-temperature simulations of magnetism through atomistic spin dynamics, which may shed further light on the magnetic ground state and its ordering temperature. Finally, the Co-Co/V-Al interface does not possess any of the intriguing features observed for the Co-Mn/Mn-Al interface. Although this makes it less interesting from a physical point of view, it also makes it more suitable for constructing heterostructures with a high spin polarization.


## ACKNOWLEDGMENTS

We thank I. E. Brumboiu for the artwork and J. Schött for performing the analytical continuation. Financial support by the DFG Research unit FOR1348 and by the Knut and Alice Wallenberg Foundation (KAW Projects No. 2013.0020 and No. 2012.0031) is gratefully acknowledged. The computations were performed on resources provided by the Swedish National Infrastructure for Computing (SNIC) at the National Supercomputer Centre (NSC) at Linköping University (Sweden).


## APPENDIX A: THE ROLE OF $U$ AND $J$

The calculations presented in the main text were also repeated using Coulomb interaction parameters for $Co_2MnAl$ as calculated in Ref. [47]. This means that $U$ ($J$) was set to 3.23 (0.6) and 3.40 (0.7) eV for, respectively, Mn and Co. In principle, there are several reasons why using directly those values does not represent a correct procedure in our computational scheme. First, these values were obtained for a localized basis set (maximally localized Wannier functions) that is different from the one used here (atomiclike functions evaluated at the linearization energy of the LMTOs; see Ref. [46] for more details). Second, neither SPTF nor LSDA+$U$ offer a proper description of the intra-3*d* screening (as a matter of fact in LSDA+$U$ there is no screening at all, being a single-particle approximation at the Hartree-Fock level). Therefore, using calculated values from cRPA would lead to a drastic overestimation of correlation effects beyond DFT.

In any case, the results obtained from these additional calculations offer a physical picture close to the one discussed in Sec. III A. We can illustrate these points with the help of Fig. 13, where DOS and PDOS for all the relevant states are reported. As a consequence of a larger value of $U$, LSDA+$U$

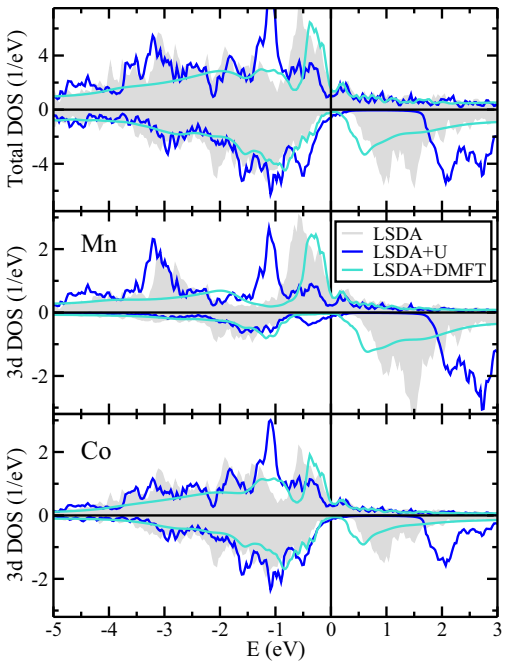


FIG. 13. As Fig. 1, but for different values of $U$ and $J$.

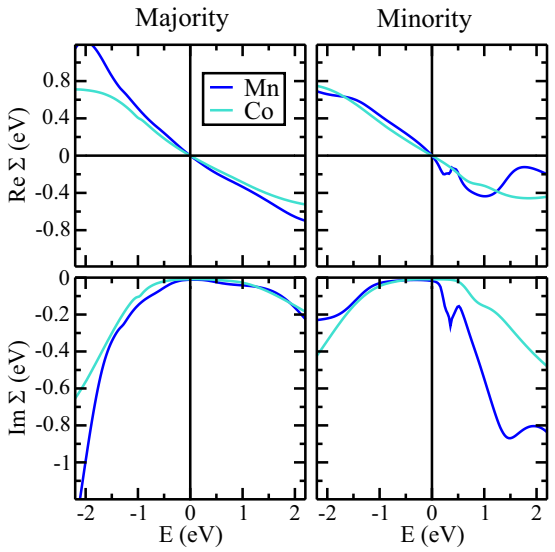


FIG. 14. As Fig. 3 but for different values of $U$ and $J$.

predicts a larger gap in the minority spin channel and the formation of a pseudogap in the majority spin channel. For even larger values of $U$, this system is likely to turn into an insulator. In LSDA+DMFT, instead, one can see that the signature of NQP states in the minority spin channel is much more evident, as a tail of states propagates from the conduction band towards the Fermi level. Even for this overestimated value of $U$, however, the half-metallic character is not broken, which confirms the whole analysis presented in the main text. Also concerning the self-energy, which is reported in Fig. 14, we do not observe qualitative differences, but just a overall increase. The peak corresponding to the NQP states retains the same magnitude but shifts slightly closer to the Fermi energy.

We also performed similar calculations for CoMnVAl, by using Coulomb interaction parameters calculated for $Co_2MnAl$ and $Mn_2VAl$ in Ref. [47]. This means that $U$ ($J$) was set to 3.23 (0.6), 3.40 (0.7), and 3.06 (0.55) eV for, respectively, Mn, Co, and V. These parameters are not ideal, not only for the reasons mentioned above, but also since $Co_2MnAl$ and $Mn_2VAl$ are both HMFs, while CoMnVAl is a SC. The physical picture emerging from LSDA+$U$ calculations is similar to the one already discussed in Sec. III B. DOS and PDOS (data not shown) are similar to the LSDA+$U$ curves reported in Fig. 5, but characterized by a slightly larger gap. The LSDA+DMFT calculations, instead, show that for this large value of $U$, CoMnVAl becomes a metal. This does not seem a realistic effect, but is likely to be due to the perturbative nature of SPTF, which is not able to treat such large values of the Coulomb

TABLE II. Site-projected and total magnetic moments for bulk $Co_2MnAl$ compared to the corresponding values (within parentheses) in the innermost layer of the HMF side of the interface. The values are expressed in $\mu_B$ and are obtained in LSDA.

| | $\mu_{Mn}$ | $\mu_{Co}$ | $\mu_{Al}$ |
|---|---|---|---|
| $Co_2MnAl$ | 2.48 (2.59) | 0.81 (0.78) | −0.03 (−0.03) |
| CoMnVAl | 0.00 (0.00) | 0.00 (0.00) | 0.00 (0.00) |

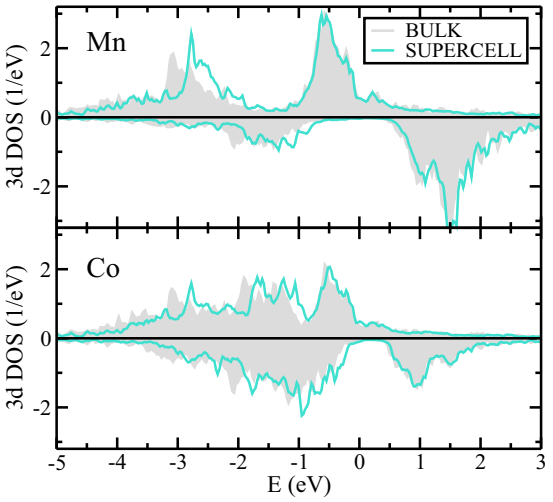


FIG. 15. PDOS for the 3$d$ states of Mn and Co, in bulk $Co_2MnAl$ (gray shade) and in the innermost layer (turquoise) of the half-metallic side of the heterostructure. Calculations were done in LSDA. Positive and negative values correspond to majority and minority spin channels, respectively. The Fermi level is at zero energy and emphasized with a vertical line.

interaction parameters in absence of magnetism. This problem has been extensively discussed in Ref. [86].

## APPENDIX B: DETAILS OF THE SUPERCELL

In this study we used a supercell of 64 atoms, shown in Fig. 7. The innermost layers of each side (component) were found to be in reasonable agreement with their corresponding

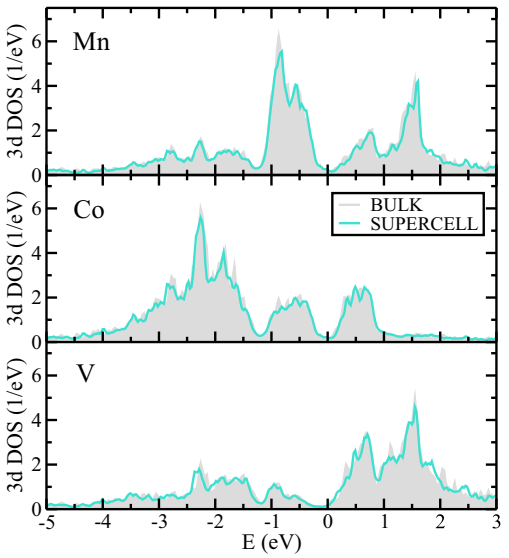


FIG. 16. PDOS for the 3$d$ states of Mn, Co, and V, in bulk CoMnVAl (gray shade) and in the innermost layer (turquoise) of the semiconducting side of the heterostructure. Calculations were done in LSDA. Positive and negative values correspond to majority and minority spin channels, respectively. The Fermi level is at zero energy and emphasized with a vertical line.

bulk systems. Magnetic moments as obtained in LSDA are reported in Table II. As one can see, the properties of bulk CoMnVAl are reproduced quite well, with all magnetic moments disappearing in the layers of the supercell which are farther from the interfaces. Concerning $Co_2MnAl$, instead, there is some discrepancy for the magnetic moment at the Mn site, which in the supercell is about 4% larger than in the bulk. The moments at the Co sites, conversely, are about 3% smaller in the supercell than in the bulk. Similar conclusions are reached by looking at the PDOSs for the electronic states of interest, which are reported in Figs. 15 and 16. The PDOS of $Co_2MnAl$ in the bulk and in the supercell show some differences, but those are mainly located far from the Fermi level and therefore do not change our qualitative analysis of the properties at the interface. Finally, projections over real spherical harmonics (not shown) illustrate that in the innermost layers the symmetry of the bulk states, which is broken at the interface, is completely recovered. Reproducing the exact crystal field splitting observed in the bulk, however, requires a few more layers of $Co_2MnAl$.


[1] D. D. Awschalom and M. E. Flatte, Nat. Phys. **3**, 153 (2007).
[2] M. N. Baibich, J. M. Broto, A. Fert, F. N. Van Dau, F. Petroff, P. Etienne, G. Creuzet, A. Friederich, and J. Chazelas, Phys. Rev. Lett. **61**, 2472 (1988).
[3] G. Binasch, P. Grünberg, F. Saurenbach, and W. Zinn, Phys. Rev. B **39**, 4828 (1989).
[4] R. A. de Groot, F. M. Mueller, P. G. van Engen, and K. H. J. Buschow, Phys. Rev. Lett. **50**, 2024 (1983).
[5] R. A. de Groot, Physica B (Amsterdam) **172**, 45 (1991).
[6] R. A. de Groot, A. M. van der Kraan, and K. H. J. Buschow, J. Magn. Magn. Mater. **61**, 330 (1986).
[7] J. H. Wijngaard, C. Haas, and R. A. de Groot, Phys. Rev. B **40**, 9318 (1989).
[8] R. Farshchi and M. Ramsteiner, J. Appl. Phys. **113**, 191101 (2013).
[9] P. Hohenberg and W. Kohn, Phys. Rev. **136**, B864 (1964).
[10] W. Kohn and L. J. Sham, Phys. Rev. **140**, A1133 (1965).
[11] W. Kohn, Rev. Mod. Phys. **71**, 1253 (1999).
[12] M. I. Katsnelson, V. Y. Irkhin, L. Chioncel, A. I. Lichtenstein, and R. A. de Groot, Rev. Mod. Phys. **80**, 315 (2008).
[13] D. M. Edwards and J. A. Hertz, J. Phys. F **3**, 2191 (1973).
[14] V. Y. Irkhin and M. I. Katsnelson, J. Phys.: Condens. Matter **2**, 7151 (1990).
[15] V. Y. Irkhin and M. I. Katsnelson, Phys. Usp. **37**, 659 (1994).
[16] L. Chioncel, Y. Sakuraba, E. Arrigoni, M. I. Katsnelson, M. Oogane, Y. Ando, T. Miyazaki, E. Burzo, and A. I. Lichtenstein, Phys. Rev. Lett. **100**, 086402 (2008).
[17] V. Y. Irkhin and M. I. Katsnelson, Eur. Phys. J. B **30**, 481 (2002).
[18] E. McCann and V. I. Fal'ko, Phys. Rev. B **68**, 172404 (2003).
[19] G. Tkachov, E. McCann, and V. I. Fal'ko, Phys. Rev. B **65**, 024519 (2001).
[20] E. McCann and V. I. Fal'ko, Phys. Rev. B **66**, 134424 (2002).
[21] V. Y. Irkhin and M. I. Katsnelson, Phys. Rev. B **73**, 104429 (2006).
[22] W. Metzner and D. Vollhardt, Phys. Rev. Lett. **62**, 324 (1989).
[23] A. Georges, G. Kotliar, W. Krauth, and M. J. Rozenberg, Rev. Mod. Phys. **68**, 13 (1996).
[24] G. Kotliar and D. Vollhardt, Phys. Today **57**, 53 (2004).
[25] G. Kotliar, S. Y. Savrasov, K. Haule, V. S. Oudovenko, O. Parcollet, and C. A. Marianetti, Rev. Mod. Phys. **78**, 865 (2006).
[26] L. Chioncel, M. I. Katsnelson, R. A. de Groot, and A. I. Lichtenstein, Phys. Rev. B **68**, 144425 (2003).
[27] L. Chioncel, M. I. Katsnelson, G. A. de Wijs, R. A. de Groot, and A. I. Lichtenstein, Phys. Rev. B **71**, 085111 (2005).
[28] L. Chioncel, E. Arrigoni, M. I. Katsnelson, and A. I. Lichtenstein, Phys. Rev. Lett. **96**, 137203 (2006).
[29] L. Chioncel, H. Allmaier, E. Arrigoni, A. Yamasaki, M. Daghofer, M. I. Katsnelson, and A. I. Lichtenstein, Phys. Rev. B **75**, 140406 (2007).
[30] J. Chico, S. Keshavarz, Y. Kvashnin, M. Pereiro, I. Di Marco, C. Etz, O. Eriksson, A. Bergman, and L. Bergqvist, Phys. Rev. B **93**, 214439 (2016).
[31] L. Chioncel, E. Arrigoni, M. I. Katsnelson, and A. I. Lichtenstein, Phys. Rev. B **79**, 125123 (2009).
[32] M. Potthoff, M. Aichhorn, and C. Dahnken, Phys. Rev. Lett. **91**, 206402 (2003).
[33] M. Potthoff, Eur. Phys. J. B **36**, 335 (2003).
[34] M. Aichhorn and E. Arrigoni, Europhys. Lett. **72**, 117 (2005).
[35] M. Aichhorn, E. Arrigoni, M. Potthoff, and W. Hanke, Phys. Rev. B **74**, 024508 (2006).
[36] H. Allmaier, L. Chioncel, E. Arrigoni, M. I. Katsnelson, and A. Lichtenstein, J. Optoelectron. Adv. Mater. **10**, 1671 (2008).
[37] H. Allmaier, L. Chioncel, E. Arrigoni, M. I. Katsnelson, and A. I. Lichtenstein, Phys. Rev. B **81**, 054422 (2010).
[38] R. Fetzer, B. Stadtmüller, Y. Ohdaira, H. Naganuma, M. Oogane, Y. Ando, T. Taira, T. Uemura, M. Yamamoto, M. Aeschlimann, and M. Cinchetti, Sci. Rep. **5**, 8537 (2015).
[39] S. Chadov, T. Graf, K. Chadova, X. Dai, F. Casper, G. H. Fecher, and C. Felser, Phys. Rev. Lett. **107**, 047202 (2011).
[40] J. M. Wills, M. Alouani, P. Andersson, A. Delin, O. Eriksson, and O. Grechnyev, *Full-Potential Electronic Structure Method* (Springer, Berlin, Heidelberg, 2010).
[41] http://fplmto-rspt.org.
[42] J. P. Perdew and Y. Wang, Phys. Rev. B **45**, 13244 (1992).
[43] J. P. Perdew, K. Burke, and M. Ernzerhof, Phys. Rev. Lett. **77**, 3865 (1996).
[44] V. I. Anisimov, F. Aryasetiawan, and A. I. Lichtenstein, J. Phys.: Condens. Matter **9**, 767 (1997).
[45] A. B. Shick, V. Drchal, and L. Havela, Europhys. Lett. **69**, 588 (2005).
[46] A. Grechnev, I. Di Marco, M. I. Katsnelson, A. I. Lichtenstein, J. Wills, and O. Eriksson, Phys. Rev. B **76**, 035107 (2007).
[47] E. Şaşıoğlu, I. Galanakis, C. Friedrich, and S. Blügel, Phys. Rev. B **88**, 134402 (2013).
[48] F. Aryasetiawan, K. Karlsson, O. Jepsen, and U. Schönberger, Phys. Rev. B **74**, 125106 (2006).
[49] T. Miyake and F. Aryasetiawan, Phys. Rev. B **77**, 085122 (2008).

[50] A. G. Petukhov, I. I. Mazin, L. Chioncel, and A. I. Lichtenstein, Phys. Rev. B **67**, 153106 (2003).
[51] E. R. Ylvisaker, W. E. Pickett, and K. Koepernik, Phys. Rev. B **79**, 035103 (2009).
[52] A. I. Liechtenstein, V. I. Anisimov, and J. Zaanen, Phys. Rev. B **52**, R5467 (1995).
[53] M. I. Katsnelson and A. I. Lichtenstein, Eur. Phys. J. B **30**, 9 (2002).
[54] I. Di Marco, J. Minár, S. Chadov, M. I. Katsnelson, H. Ebert, and A. I. Lichtenstein, Phys. Rev. B **79**, 115111 (2009).
[55] L. V. Pourovskii, M. I. Katsnelson, and A. I. Lichtenstein, Phys. Rev. B **72**, 115106 (2005).
[56] J. Schött, I. L. M. Locht, E. Lundin, O. Grånäs, O. Eriksson, and I. Di Marco, Phys. Rev. B **93**, 075104 (2016).
[57] K. S. D. Beach, R. J. Gooding, and F. Marsiglio, Phys. Rev. B **61**, 5147 (2000).
[58] O. Grånäs, I. Di Marco, P. Thunström, L. Nordström, O. Eriksson, T. Björkman, and J. M. Wills, Comput. Mater. Sci. **55**, 295 (2012).
[59] A. Liechtenstein, M. Katsnelson, V. Antropov, and V. Gubanov, J. Magn. Magn. Mater. **67**, 65 (1987).
[60] M. I. Katsnelson and A. I. Lichtenstein, Phys. Rev. B **61**, 8906 (2000).
[61] Y. O. Kvashnin, O. Grånäs, I. Di Marco, M. I. Katsnelson, A. I. Lichtenstein, and O. Eriksson, Phys. Rev. B **91**, 125133 (2015).
[62] G. Kresse and D. Joubert, Phys. Rev. B **59**, 1758 (1999).
[63] G. Kresse and J. Furthmüller, Comput. Mater. Sci. **6**, 15 (1996).
[64] K. H. J. Buschow and P. G. van Engen, J. Mag. Magn. Matter. **25**, 90 (1981).
[65] X. Zhu, E. Jiang, Y. Dai, and C. Luo, J. Alloys Compd. **632**, 528 (2015).
[66] J. Kübler, G. H. Fecher, and C. Felser, Phys. Rev. B **76**, 024414 (2007).
[67] X. Jia, W. Yang, M. Qin, and L. Wang, J. Phys. D **41**, 085004 (2008).
[68] D. Comtesse, B. Geisler, P. Entel, P. Kratzer, and L. Szunyogh, Phys. Rev. B **89**, 094410 (2014).
[69] P. J. Webster and K. R. A. Ziebeck, in *Alloys and Compounds of d-Elements with Main Group Elements. Part 2*, edited by H. P. J. Wijn (Springer, Heidelberg, 1988), Vol. 19C, pp. 104–185.
[70] L. Basit, G. H. Fecher, S. Chadov, B. Balke, and C. Felser, Eur. J. Inorg. Chem., **2011**, 3950 (2011).
[71] J. C. Slater, Phys. Rev. **49**, 931 (1936).
[72] L. Pauling, Phys. Rev. **54**, 899 (1938).
[73] M. Tas, E. Şaşıoğlu, I. Galanakis, C. Friedrich, and S. Blügel, Phys. Rev. B **93**, 195155 (2016).
[74] K. Özdoğan, E. Şaşıoğlu, and I. Galanakis, J. Appl. Phys. **113**, 193903 (2013).
[75] L. Y. Wang, X. F. Dai, X. T. Wang, Y. T. Cui, E. K. Liu, W. H. Wang, G. H. Wu, and G. D. Liu, Mater. Res. Express **2**, 106101 (2015).
[76] G. A. de Wijs and R. A. de Groot, Phys. Rev. B **64**, 020402 (2001).
[77] P. Mavropoulos, I. Galanakis, and P. H. Dederichs, J. Phys.: Condens. Matter **16**, 4261 (2004).
[78] S. Picozzi, A. Continenza, and A. J. Freeman, J. Phys. Chem. Solids **64**, 1697 (2003).
[79] P. Mavropoulos, M. Ležaić, and S. Blügel, Phys. Rev. B **72**, 174428 (2005).
[80] S. J. Hashemifar, P. Kratzer, and M. Scheffler, Phys. Rev. Lett. **94**, 096402 (2005).
[81] K. Nagao, Y. Miura, and M. Shirai, Phys. Rev. B **73**, 104447 (2006).
[82] V. Ko, G. Han, J. Qiu, and Y. P. Feng, Appl. Phys. Lett. **95**, 202502 (2009).
[83] I. Galanakis, P. Mavropoulos, and P. H. Dederichs, J. Phys. D: Appl. Phys. **39**, 765 (2006).
[84] C. Etz, L. Bergqvist, A. Bergman, A. Taroni, and O. Eriksson, J. Phys.: Condens. Matter **27**, 243202 (2015).
[85] O. Eriksson, A. Bergman, L. Bergqvist, and J. Hellsvik, *Atomistic Spin Dynamics: Foundations and Applications* (Oxford University Press, Oxford, 2017).
[86] I. Di Marco, J. Minár, J. Braun, M. I. Katsnelson, A. Grechnev, H. Ebert, A. I. Lichtenstein, and O. Eriksson, Eur. Phys. J. B **72**, 473 (2009).